Imaging compact boson stars with hot spots and thin accretion disks

João Luís Rosa[1,2,*] Caio F. B. Macedo[3,†] and Diego Rubiera-Garcia[4,‡]

[1]*University of Gdańsk, Jana Bażyńskiego 8, 80-309 Gdańsk, Poland*
[2]*Institute of Physics, University of Tartu, W. Ostwaldi 1, 50411 Tartu, Estonia*
[3]*Faculdade de Física, Campus Salinópolis, Universidade Federal do Pará,*
68721-000, Salinópolis, Pará, Brazil
[4]*Departamento de Física Teórica and IPARCOS, Universidad Complutense de Madrid,*
E-28040 Madrid, Spain

In this work we consider the observational properties of compact boson stars with self-interactions orbited by isotropically emitting (hot-spot) sources and optically thin accretion disks. We consider two families of boson stars supported by quartic and sixth-order self-interaction potentials, and choose three samples of each of them in growing compactness; only those with large enough compactness are capable to hold light rings, namely, null bound orbits. For the hot spots, using inclination angles $\theta = \{20°, 50°, 80°\}$ we find a secondary track plunge-through image of photons crossing the interior of the boson star, which can be further decomposed into additional images if the star is compact enough. For accretion disks we find that the latter class of stars actually shows a sequence of additional secondary images in agreement with the hot-spot analysis, a feature absent in typical black hole space-times. Furthermore, we also find a shadowlike central brightness depression for some of these stars in both axial observations and at the inclination angles above. We discuss our findings in relation to the capability of boson stars to effectively act as black hole mimickers in their optical appearances as well as potential observational discriminators.

I. INTRODUCTION

The Kerr hypothesis establishes the universality of the celebrated Kerr solution [1] to describe the end state of full gravitational collapse in terms of the formation of a black hole entirely described for external observers by its mass and angular momentum [2]. Analytical and computational investigations upon its background successfully reproduce current observations of gravitational wave profiles out of binary mergers [3,4] as well as the features of the strong light deflection around the supermassive objects at the heart of the M87 [5] and Milky Way [6] galaxies. This way, the existence of black holes is taken as yet another success of Einstein's general relativity to accurately describe our Universe and the objects living in it [7,8].

Nonetheless, given the (arguable) impossibility of directly observing the most salient feature of black holes—its event horizon—as well as the theoretical and observational uncertainties and inherent bias in the interpretation of gravitational waves and shadow observations,

in the past few years an entire field of *black hole mimickers* has blossomed (see [9] for a review of their observational status). These black hole mimickers usually are ultracompact objects potentially capable of disguising themselves as black holes despite not having an event horizon. Among them, boson stars—hypothetical macroscopic Bose-Einstein condensates—bear a special place. This is so because they are supported by complex scalar fields with canonical kinetic and potential terms but, more importantly, because mechanisms for their dynamical generation are known [10–12], thus overlooking the main criticisms applied to other popular black hole mimickers such as wormholes. Furthermore, they allow for a large flexibility in their implementation with scalar and vector fields [13] sustained by different classes of self-interactions, and with important phenomenological repercussions in x-ray spectroscopy [14], the dark matter problem [15,16], or gravitational wave signatures [17], echoes [18] and astrometric measurements [19].

While gravitational wave observations currently focus on stellar-mass black holes only (while we await the arrival of LISA and Einstein Telescope devices), shadow observations explore an entire different mass range, namely that of millions of solar masses upwards. Recently, many studies have recognized the great

*joaoluis92@gmail.com
†caiomacedo@ufpa.br
‡drubiera@ucm.es

opportunity to look for observational hints of black hole mimickers (including boson stars) hidden in shadow images [20–26]. Such images are created by highly bent trajectories of light rays issued by the accretion disk partnering the compact object, and which consists on a wide ring of radiation (the light ring) enclosing a central brightness depression (the shadow). Such features are strongly linked to yet another salient feature of the Kerr black hole, namely the existence of unstable null bound orbits, identified as light rings, which are a generic feature of asymptotically flat black holes [27] but can also be sustained by other ultracompact objects. Whether (i) a black hole mimicker without such bound orbits can still mimic the observed light-ring/shadow features in the images of a black hole and (ii) new features may arise that effectively act as observational discriminators between a black hole and its mimicker, are under heavy scrutiny in the literature. The most succulent feature to carry out these tasks is the sequence of additional images in which the secondary images and the light ring can be decomposed into, depending on the properties of the orbiting material [28–30], and the presence/absence of a shadow including its (calibrated) size [31,32].

The main aim of this work is to analyze the features above by imaging two families of spherically symmetric compact boson stars supported by quartic and sixth-order self-interaction terms using two methods: the observational properties of hot spots (bright regions associated to temperature anisotropies of the nonhomogeneous accretion flow [33]) orbiting the boson star, and those of optically and geometrically thin accretion disks, emitting isotropically. This analysis brings out the succulent observational features of these objects. Indeed, for the first method we observe a secondary track, plunge-through trajectory, on top of the primary track of the hot spot in the integrated fluxes of those boson stars, which can be further decomposed into additional secondary tracks for large enough compactness, a feature that becomes more acute for larger observational angles, in agreement with previous results [34]. This neatly distinguishes some of our configurations from canonical black holes and triggers new observational opportunities. Indeed, when using the second method for such very compact boson stars when illuminated by well-motivated intensity profiles, we find two interesting features of some of these objects: (i) a sequence of new secondary images that do not appear in their black hole counterparts and (ii) a shadowlike feature, i.e., a central brightness depression. While the first such feature is in agreement with the one found in the hot spots and may act as a clear observational discriminator between boson stars and black holes, the second allows such boson stars to effectively act as black hole mimickers, even at large observation inclination angles.

This work is organized as follows: in Sec. II we set our theoretical framework and specify the three plus three configurations of boson stars supported by quartic and sixth-order self-interactions with different compactnesses, respectively, develop the equations for geodesic motion and discuss the stability of timelike orbits. In Sec. III, we consider the observational properties of hot spots analyzing the integrated fluxes and astrometrical quantities at observation angles $\theta = \{20°, 50°, 80°\}$. In Sec. IV we consider the observational properties of these boson stars when illuminated by a geometrically and optically thin accretion disk, placing the focus on the multiring structure and the shadowlike mimicking features of some of these stars at both axial inclination and the observational inclinations mentioned above. In Sec. V we conclude with a summary and critical discussion of our results.

II. THEORETICAL FRAMEWORK

A. Models and configurations

Let us a consider a (complex) scalar field Φ minimally coupled to the gravitational field via the action ($a = 0, 1, 2, 3$)

$$S = \int d^4x \sqrt{-g} \left[\frac{R}{16\pi} - \frac{1}{2} \partial_a \Phi^* \partial^a \Phi - \frac{1}{2} V(|\Phi|^2) \right], \quad (1)$$

where g is the determinant of the space-time metric $g_{\mu\nu}$ written in terms of a coordinate system x^a, R is the Ricci scalar, a star Φ^* denotes a complex conjugate, and V is the scalar potential. We have adopted a system of geometrized units for which $G = c = 1$. The corresponding field equations are obtained by varying Eq. (1) with respect to the metric g_{ab} and the scalar field Φ to yield

$$G_{ab} = 8\pi T_{ab}, \quad (2)$$

$$\nabla_a \nabla^a \Phi = \frac{dV}{d|\Phi|^2} \Phi, \quad (3)$$

where T_{ab} is the stress-energy tensor of the complex scalar field Φ and it is given by

$$T_{ab} = \frac{1}{2} (\nabla_a \Phi^* \nabla_b \Phi + \nabla_b \Phi^* \nabla_a \Phi) - \frac{1}{2} g_{ab} (\nabla_c \Phi^* \nabla^c \Phi + V), \quad (4)$$

where ∇_c denotes covariant differentiation. We are interested here in considering static and spherically symmetric boson stars, and thus we consider the ansatz for the metric,

$$ds^2 = -A(r)dt^2 + B(r)^{-1}dr^2 + r^2 d\Omega^2, \quad (5)$$

$$\Phi = \phi(r)e^{-i\omega t}, \quad (6)$$

where we have introduced the metric functions $A(r)$, $B(r)$, while $\phi(r)$ characterizes the radial part of the scalar field,

with ω denoting its frequency, and $d\Omega^2$ denotes the line element on the two-sphere. Replacing this ansatz into the field equations in Eqs. (2) and (3) leads to the equations of motion of the system (a prime denotes a radial derivative):

$$\frac{rB' + B - 1}{r^2} = -2\pi\left(\frac{w^2\phi^2}{A} + B\phi'^2 + V\right), \qquad (7)$$

$$\frac{\frac{BrA'}{A} + B - 1}{r^2} = 2\pi\left(\frac{w^2\phi^2}{A} + B\phi'^2\right), \qquad (8)$$

$$\frac{1}{2}\phi'\left(B\left(\frac{A'}{A} + \frac{4}{r}\right) + B'\right) + \phi\left(\frac{w^2}{A} - \frac{dV}{d|\phi|^2}\right) + B\phi'' = 0. \qquad (9)$$

This is a highly nonlinear system whose resolution demands the employment of suitable numerical methods. To this end, we supply asymptotic boundary conditions by demanding asymptotic flatness of the geometry via a Schwarzschild-like behavior, and a vanishing radial scalar field at $r \to \infty$, that is

$$A(r \to \infty) = 1 - \frac{2M}{r}, \qquad (10)$$

$$B(r \to \infty) = 1 - \frac{2M}{r}, \qquad (11)$$

$$\phi(r \to \infty) = 0, \qquad (12)$$

where M is the total mass of the boson star. At the origin we demand the metric functions to be normalized to a finite value, and the radial scalar field to a target value ϕ_c, i.e.,

$$A(r \approx 0) = A_c, \qquad (13)$$

$$B(r \approx 0) = 1, \qquad (14)$$

$$\phi(r \approx 0) = \phi_c, \quad \text{and} \quad \phi'(r \approx 0) = 0. \qquad (15)$$

In practice, we can always set $A_c = 1$ through a time reparametrization. This leads to a background that does not asymptotically match Eq. (10). Upon finishing the integration, we rescale the time coordinate (changing ω and A) to obtain the space-time solution in the usual Schwarzschild-like coordinates. Therefore, we integrate the differential equations [Eqs. (2) and (3)] for static and spherically symmetric backgrounds from the origin using the boundary conditions in Eqs. (13)–(15). In order to do so, we must first specify the scalar potential. In what follows, we consider two well-motivated potentials:

(i) $V = \mu^2|\Phi|^2 + \Lambda|\Phi|^4$ [35], where μ is the mass term and Λ is a coupling constant. Boson stars (BSs) presenting quartic self-interactions can be highly massive objects as the maximum mass configuration

TABLE I. Boson star configurations used in this paper. We select three different solutions for each model: {ΛBS1, ΛBS2, ΛBS3} for the Λ stars, and {SBS1, SBS2, SBS3} for the solitonic stars. The parameters are ϕ_c for the central scalar field, μ for the mass term, R for the radius of the star, M for its mass, $\mathcal{C} \equiv M/R$ for the compactness (for a Schwarzschild black hole, $\mathcal{C} = 1/2$), and ω for the scalar field frequency.

Configuration	ϕ_c	μM	μR	$\mathcal{C}$	ω/μ
ΛBS1	0.03045	1.6321	16.1577	0.10101	0.88124
ΛBS2	0.03457	1.7356	14.9648	0.11597	0.86410
ΛBS3	0.04582	1.8368	12.4524	0.14750	0.82786
SBS1	0.0827	1.7531	11.5430	0.1518	0.25827
SBS2	0.0827	4.220	16.6520	0.25342	0.17255
SBS3	0.0850	5.655	17.6470	0.32045	0.13967

scales with Λ as $M_{\max} \sim \Lambda^{1/2}m_p^3/\mu^2$ for large values of Λ. However, the compactness of these solutions saturates for large Λ, with the boson stars radius R never being smaller than $6M$. This implies that all circular orbits with orbital radii $r_o > 0$ are stable independently of the value of Λ [36]. We shall denote this class of models as ΛBS.

(ii) $V = \mu^2|\Phi|^2(1 + |\Phi|^2/\alpha^2)^2$ [37], where α is a constant parameter. Potentials of this type allow for (degenerate) vacuum configurations. This potential is usually labeled as solitonic, and its self-gravitating solutions as solitonic boson stars (SBSs) as it is one of the simplest potentials that feature nontopological solitons in the absence of gravity. In this case, ultracompact solutions can be achieved in the limit $\alpha \to 0$, with the minimum radius being $R \approx 2.81M$ [38,39]. Because of their compactness, solitonic BSs can have light rings, being an interesting candidate as a spherical black hole mimicker [40].

In this work we consider three candidates belonging to each ΛBS and SBS class, whose chosen parameters and main features are displayed in Table I. We focus on the values $\Lambda = 400$ and $\alpha = 0.08$, picking three solutions for each potential, all of which are linearly stable against radial perturbations. We depict in Fig. 1 the behavior of the metric and scalar field functions, and in Fig. 2 the corresponding mass-radius relations, highlighting with markers the solutions explored in this paper. As the scalar field $\phi(r)$ decays exponentially for $r \gg \mu^{-1}$ but never vanishes, a "surface" for these BSs cannot be properly defined, and one can only introduce an effective radius, which we define in such a way as to encompass 98% of its total mass. The mass function $m(r)$ can be found through

$$B(r) = 1 - \frac{2m(r)}{r}, \qquad (16)$$

and, therefore the radius is defined by $m(R) = 0.98M$. Numerical solutions for very small values of α and very large values of Λ are challenging to find with the usual
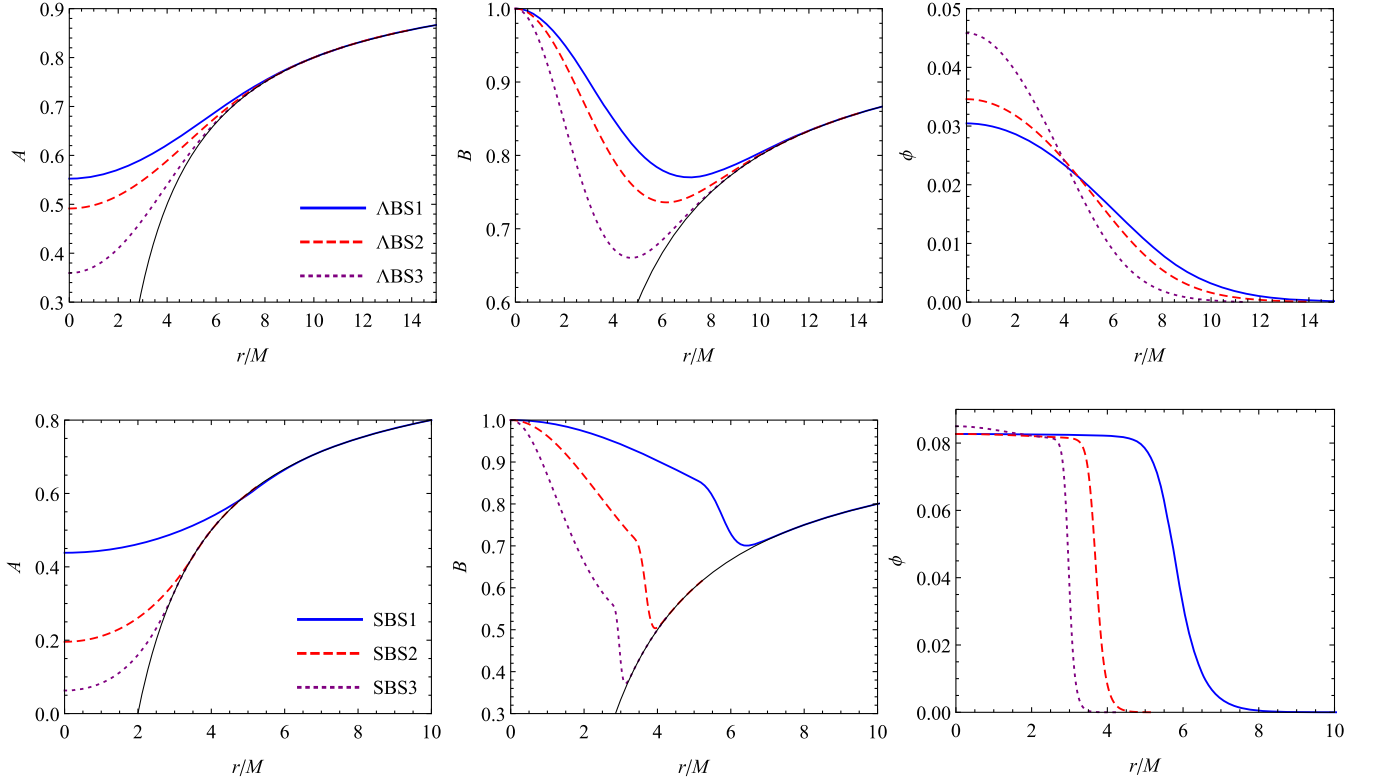
FIG. 1. Background quantities for the metric coefficients and the scalar field for the three ΛBS (top) and the three SBS (bottom) compared to the Schwarzschild black hole (thin black line).

shooting methods, but can be found via alternative semi-analytical approximations [36,38]. Nonetheless, we shall use the full numerical solutions in order to analyze the space-time, with the aid of analytical fits for the image computations.

It is important to note that, given the absence of a stable massive scalar field in the standard model of particle physics, the scalar field of which the bosonic stars in this work are composed of can be thought of as dark matter particles which only weakly (gravitationally) interact with the baryonic matter composing the astrophysical objects modeled in the upcoming sections. Therefore, in what follows, any interaction between matter and the bosonic star is neglected, see Eq. (1), including emission from the bosonic star itself, and the astrophysical objects moving in the bosonic star background are considered to follow geodesic motion.
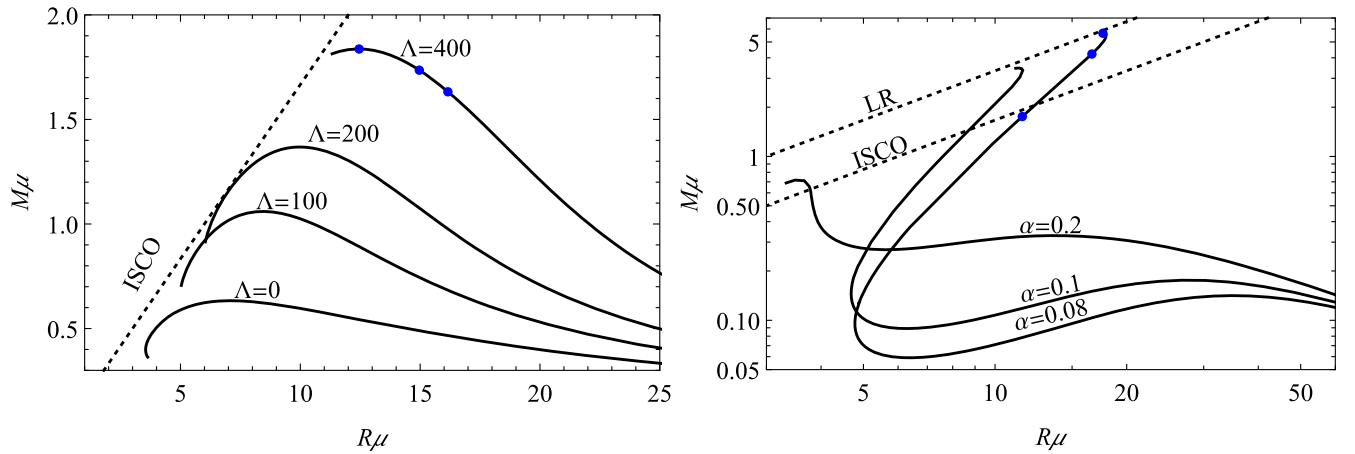

FIG. 2. Mass-radius curves for ΛBS (left) and SBS (right) configurations considering different values of the parameters. While for the ΛBS we see that the radius never crosses the ISCO region (given by $R = 6M$), the solitonic potential can generate solutions very close to the corresponding light ring in the Schwarzschild black hole ($R = 3M$). The blue markers indicate the solutions used in this paper.

B. Timelike circular geodesics, marginally stable orbits and light rings

Before going into details about the imaging of boson stars, it is instructive to study the geodesic structure of these space-times. The Lagrangian describing orbits at the equatorial plane $\theta = \pi/2$ (something we can fix without loss of generality due to the spherical symmetry of the system) is given by

$$2\mathcal{L} = -A\dot{t}^2 + B^{-1}\dot{r}^2 + r^2\dot{\varphi}^2 = -\delta, \qquad (17)$$

where the overdot indicates derivative with respect to the geodesic affine parameter, φ is the azimuthal angle, and $\delta = 1$ (0) for timelike (null) geodesics. Introducing the following definitions for the specific energy and angular momentum per unit mass, i.e.,

$$\varepsilon = -\frac{\partial\mathcal{L}}{\partial\dot{t}} = A\dot{t}, \quad \text{and} \quad \ell = \frac{\partial\mathcal{L}}{\partial\dot{\varphi}} = r^2\dot{\varphi}, \qquad (18)$$

the equation of motion for the radial coordinate is given by the effective balance equation,

$$\frac{A}{B}\dot{r}^2 = \varepsilon^2 + V_{\text{eff}}, \qquad (19)$$

where

$$V_{\text{eff}} = A\left(\delta + \frac{\ell^2}{r^2}\right) \qquad (20)$$

is the effective potential describing the geodesics. Let us consider the case of timelike circular orbits. We can use the above equations, together with the first derivatives of the effective potential, to find the specific energy and angular momentum, obtaining

$$\varepsilon^2 = \frac{2A}{2A - r_oA'}, \qquad l_P^2 = \frac{r_o^3A'}{2A - r_oA'}, \qquad (21)$$

where r_o is the radius of the circular orbit and all the quantities above are evaluated at $r = r_o$.

Note that both the specific energy and angular momentum diverge at a (possible) orbit for which

$$2A(r_o) - r_oA'(r_o) \qquad (22)$$

vanishes. If the above equation is satisfied for real values of r_o, this corresponds to the position of null circular orbits (in the Schwarzschild space-time this results in $r_o = 3M$). Note that ultracompact objects without event horizons are known for having light rings that come in pairs [41,42]. Therefore, it is instructive to track Eq. (22) to search for possible light rings. We focus on SBSs as these are the most compact objects explored in this paper. We display the
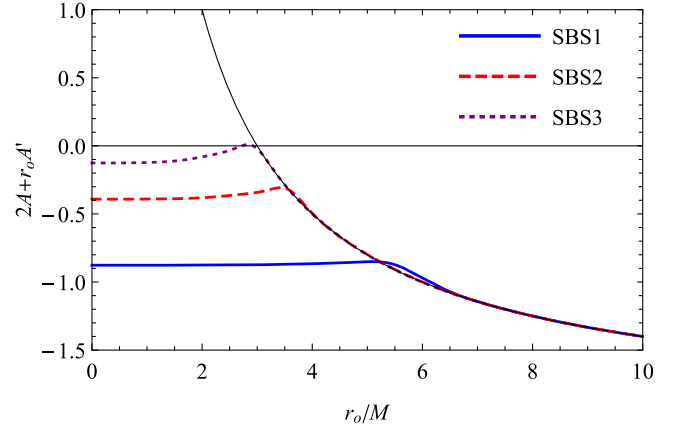

FIG. 3. Discriminator for the existence of light rings. The roots [i.e., the zeroes of $2A(r_o) - r_oA'(r_o)$], when present, correspond to the light-ring positions.

evolution of this quantity with the ratio r_o/M for the three SBS configurations presented in this work in Fig. 3. Among all models (including the ΛBS), only the SBS3 one presents such light rings (around $r_o/M \approx 3$).

Although it is physically possible to place a particle in a circular orbital motion close to light rings, this analysis does not tell us anything about the stability of such orbits. The stability of timelike circular orbits can be analyzed through the sign of the effective potential in Eq. (20), i.e.,

$$V_{\text{eff}}''\begin{cases} > 0, & \text{Stable,} \\ = 0, & \text{Marginally stable (ISCO for BH),} \\ < 0, & \text{Unstable,} \end{cases} \qquad (23)$$

provided that (ε, ℓ) are real for the orbit to exist. By analyzing the models investigated in this paper, we find that for ΛBS all circular orbits are stable, meaning that accretion disks may extend all the way down to the center of the star. For the SBS models, however, we find that there is a window in which either the orbits do not exist or are unstable. This is illustrated in Fig. 4, where we plot the second derivative of the effective potential for the SBS models. We plot this quantity logscale to illustrate solely the stable orbits. For SBS2 and SBS3, the outer marginally stable circular orbit is located very close to $6M$, similarly to the Schwarzschild black hole case. This is not surprising, as these boson stars have radius such that $R/M < 6$. Surprisingly, for SBS1, even though the configuration has radius bigger than $6M$, unstable orbits still exist. This illustrates that naively looking into the compactness only to search for marginally stable circular orbits or light rings in BSs might lead to wrong results.

In Ref. [22] it was pointed out that having stable timelike circular orbits inside the BS is not enough to determine whether a physical light source may exist in those orbits (see also Ref. [25]). A central point is the existence of a maximum in the angular frequency of the timelike
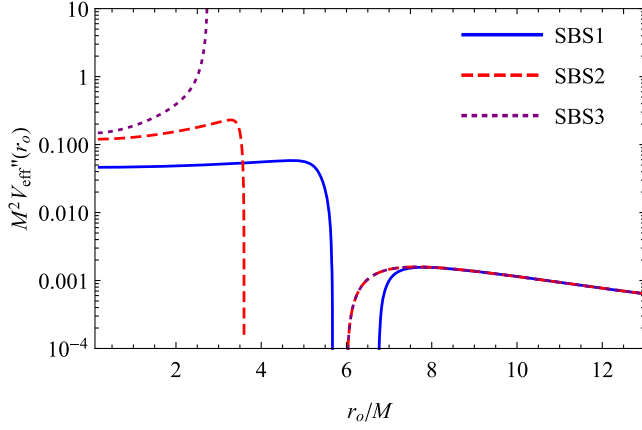
FIG. 4. Second derivative of the effective potential in Eq. (20) as a function of the orbital radius. Even the least compact SBS solution presents a window of unstable orbits, with radius larger than the corresponding innermost stable circular orbit in the Schwarzschild black hole.

geodesics Ω_o at some radius, which introduces a scale for the inner edge of the accretion disks. The angular frequency for timelike geodesics can be computed through

$$\Omega_o = \frac{\dot{\varphi}}{\dot{t}}\bigg|_{r=r_o} = \sqrt{\frac{A'(r_o)}{2r_o}}. \qquad (24)$$

In Fig. 5 we show the angular frequency for the BSs explored in this paper. We see that for the ΛBS cases (left panel of Fig. 5) the maximum of the frequency is located near the center of the star, indicating that it would be difficult for accretion disks to have a Schwarzschild-like structure. However, for all SBSs explored in this paper, a maximum in the frequency is observed (left panel of Fig. 5). This indicates that SBSs are more likely to produce accretion disk structures similar to those of black holes.
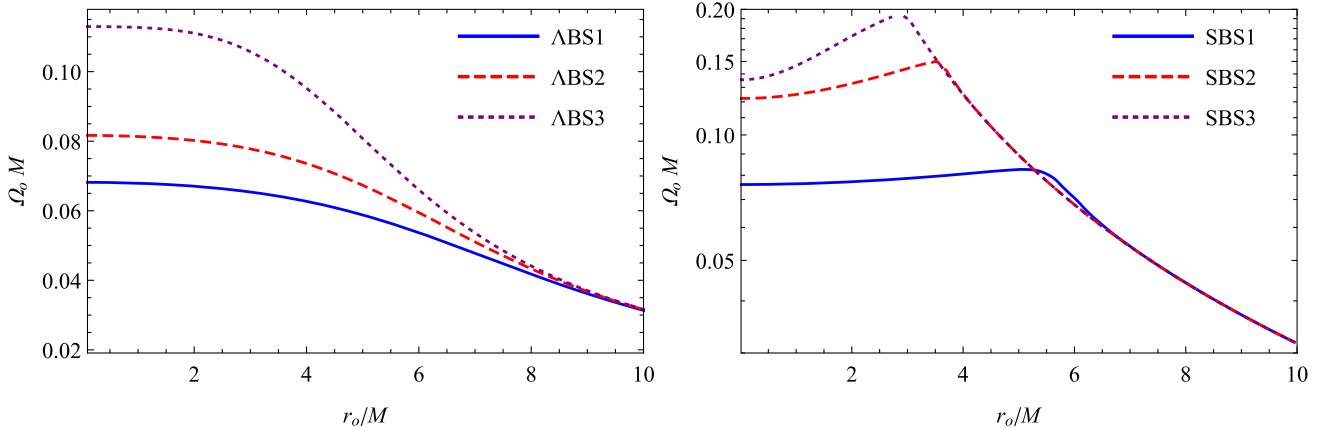
Finally, from directly integrating the geodesic equation we can illustrate how strong the lensing can be in the BSs explored in this paper. Let us focus on the most compact models for each self-interaction, i.e., ΛBS3 and SBS3. We consider a single emitter located at either $(x, y) = (2M, 0)$ or $(x, y) = (8M, 0)$, to illustrate the behavior of a source located inside and outside the star, respectively. The result is shown in Fig. 6. For a source outside the star, the ΛBS3 produces a caustic effect inside the star (something that was observed in other compact stellar models [43]) and the SBS3 model has strong deflections which are consistent with the fact that such configurations have light rings. For the source inside the star, we see that the effect in the ΛBS3 is weaker, indicating that possible observational effects from that region should be mostly due to the gravitational redshift. For the SBS3 model, however, we can see strong deflections even for a source located inside the star, which combined with the strong redshift due to its compactness should provide a strong candidate to mimic black hole images. In the bottom panels of Fig. 6 we show how light rays reach a distant observer, considering a parallel stream coming far from the star. These rays would correspond to pixels in the observed image and, therefore, give a notion of how the image would be formed. We shall further investigate more physical sources in the next sections.

III. ORBITS AND HOT SPOTS

Let us now analyze the observational properties of hot spots orbiting a central bosonic star, the latter described by the ΛBS and SBS configurations described in the previous section. For this purpose, we recur to the ray-tracing open-source code GYOTO [44], on which we model the hot spot as an isotropically emitting spherical source orbiting the central object at some constant orbital radius r_0 and at the
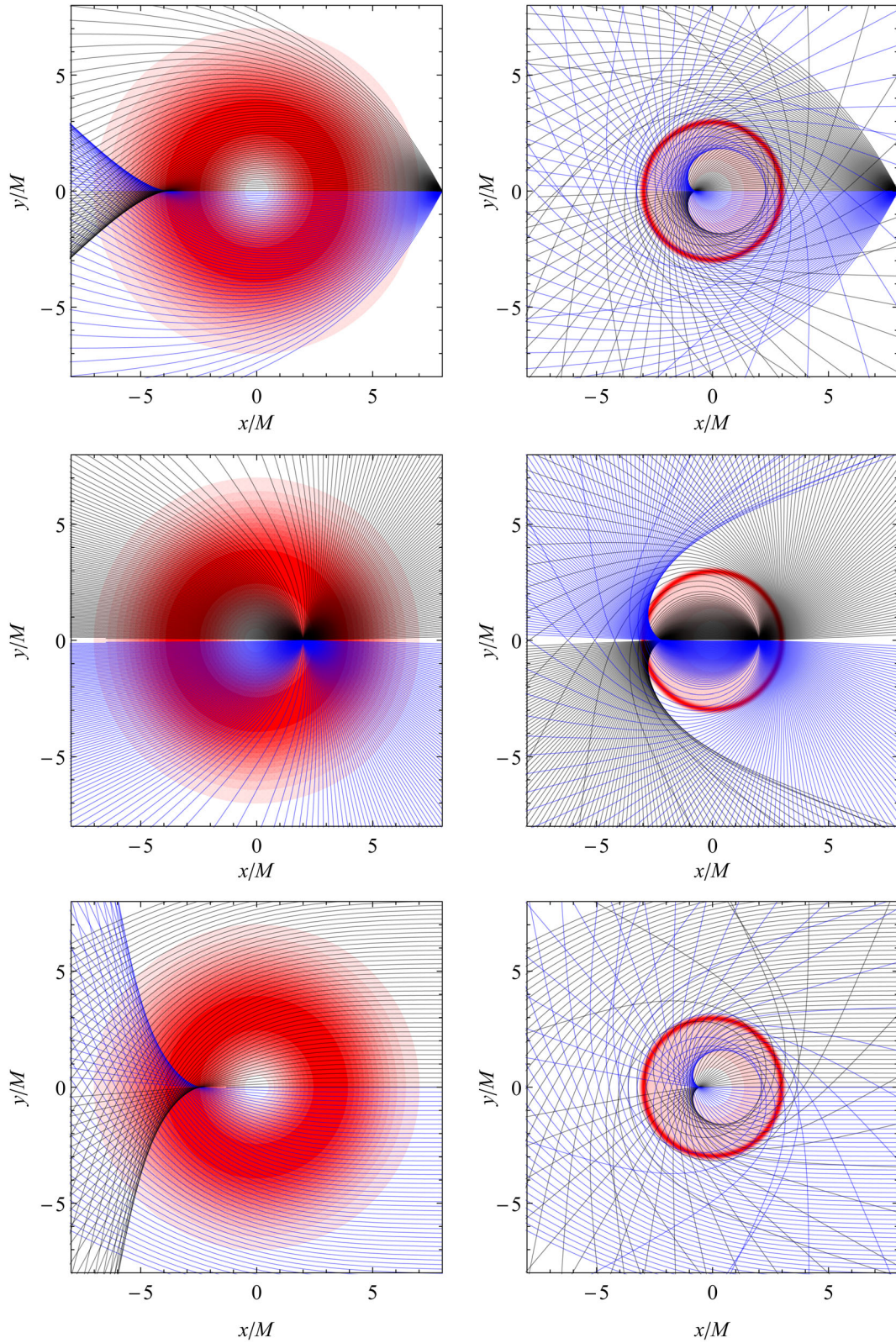

FIG. 5. Angular frequency for timelike circular geodesic motion for the different boson star configurations explored in this paper. Left panel: for ΛBS all timelike circular geodesics are stable and present a maximum close to the center of the star. Right panel: for SBSs however, the maximum frequency is always at some finite radius. We stress here that not all of these orbits are stable (as indicated in Fig. 4). Moreover, for the SBS3 orbits there is a forbidden region in between the light rings.

FIG. 6. Light-ray deflections by the ΛBS 3 (left panel) and the SBS3 (right panel) assuming an emitter located at $(x, y) = (8M, 0)$ (top panels) and $(x, y) = (2M, 0)$ (middle panels). The bottom panel considers light rays that reach an observer far from the star and, therefore, illustrate how the configuration would be visualized at that region. The contour plot represents the derivative of the mass function, which decreases exponentially near the stellar radius.
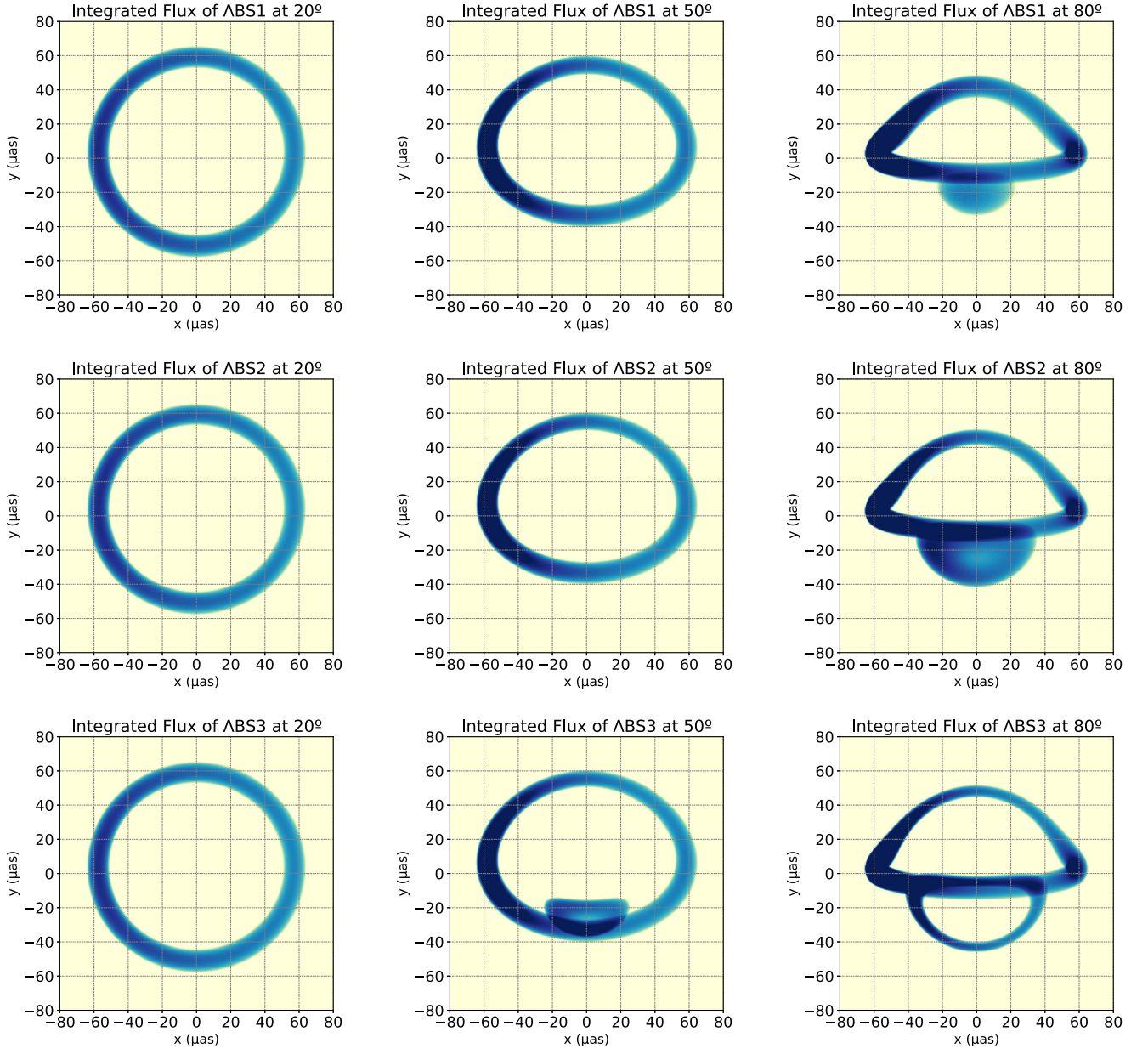
FIG. 7. Normalized integrated flux of the observations for the ΛBS models, namely ΛBS1 (top row), ΛBS2 (middle row), and ΛBS3 (bottom row), for an observation inclination of $\theta = 20°$ (left column), $\theta = 50°$ (middle column), and $\theta = 80°$ (right column).

equatorial plane, i.e., $\theta = \pi/2$.[1] As a run test, we use this software to ray trace light trajectories in the two most compact configurations considered in this work, namely, ΛBS3 and SBS3, which are depicted in Fig. 6 (left and right plots, respectively).

For the sake of this work, we have set the orbital radius to $r_o = 8M$ and the radius of the hot spot to $r_H = M$, where M is the Arnowitt-Deser-Misner (ADM) mass of the background space-time, which is taken to be the mass of

Sgr A*, i.e., $M = 4.26 \times 10^6 M_\odot$, where $M_\odot$ is the solar mass. Furthermore, the distance from the center of the object to the observer is taken to be the distance from the Sun to Sgr A*. i.e., $d = 8.25$ kpc. Under these assumptions, GYOTO outputs a two-dimensional matrix of specific intensities I_{lm}^ν at a given time instant t_k. This matrix can be interpreted as an observed image, where each of the pixels $\{m, l\}$ is associated with an observed intensity. The simulation is then repeated through several time instants $t_k \in [0, T[$, where T is the orbital period of the hot spot, to obtain cubes of data $I_{klm} = \delta\nu I_{lm}^\nu$, where $\Delta\nu$ is the spectral width. We use these simulated cubes of data to produce three observables, namely,

---

[1]In practice, this is implemented in GYOTO through the astrophysical object class *Gyoto::Astrobj::Star*. More information regarding this model can be found in GYOTO's official website.

(1) Time integrated fluxes:

$$\langle I \rangle_{lm} = \sum_k I_{klm}, \qquad (25)$$

(2) Temporal fluxes:

$$F_k = \sum_l \sum_m \Delta\Omega I_{klm}, \qquad (26)$$

(3) Temporal centroids:

$$\vec{c}_k = \frac{1}{F_k} \sum_l \sum_m \Delta\Omega I_{klm} \vec{r}_{lm}, \qquad (27)$$

where $\Delta\Omega$ is the solid angle of a single pixel and $\vec{r}_{lm}$ is a vector representing the displacement of the pixel $\{l, m\}$ with respect to the center of the observed image. A more popular astronomical observable, the temporal magnitude m_k, can then be obtained from the temporal flux F_k, as

$$m_k = -2.5 \log\left(\frac{F_k}{\min(F_k)}\right). \qquad (28)$$

In Figs. 7 and 8 we show the integrated fluxes for the three ΛBS and the three SBS, respectively, as observed through three different inclination angles with respect to the vertical axis, chosen conveniently as $\theta = \{20°, 50°, 80°\}$.
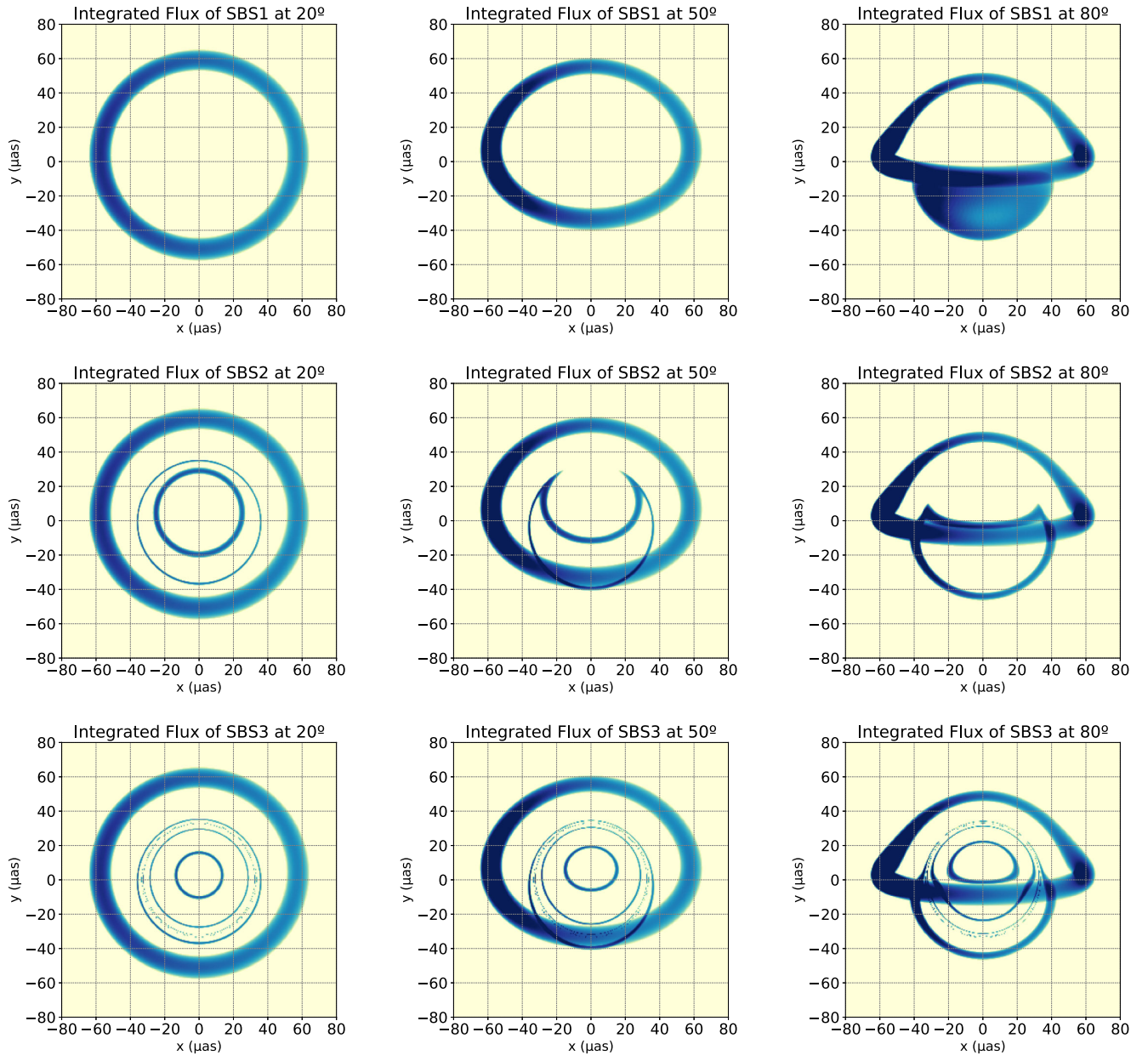

FIG. 8. Normalized integrated flux of the observations for the SBS models, namely SBS1 (top row), SBS2 (middle row), and SBS3 (bottom row), for an observation inclination of $\theta = 20°$ (left column), $\theta = 50°$ (middle column), and $\theta = 80°$ (right column).
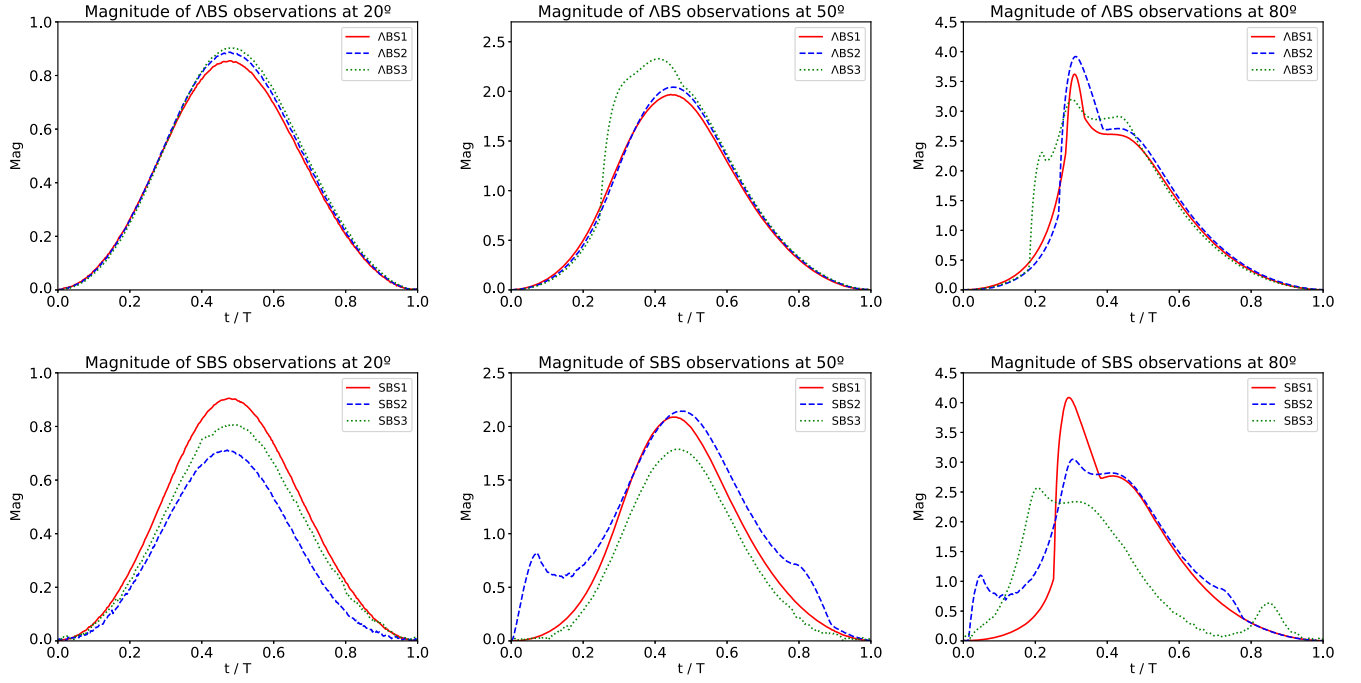
FIG. 9.   Normalized magnitude of the observations in arbitrary units as a function of t/T for the ΛBS models (top row) and the SBS models (bottom row) for an observation inclination of $\theta = 20°$ (left column), $\theta = 50°$ (middle column), and $\theta = 80°$ (right column).

The magnitudes for the same solutions and observation angles are plotted in Fig. 9, and the corresponding centroids are plotted in Fig. 10. In these two latter figures, we also provide a comparison between the three ΛBS solutions and the three SBS solutions for different inclination angles, in order to allow one to observe how an increase in the compactness of the bosonic star configuration affects its observables. In the following subsections, we analyze separately the integrated fluxes and the astrometrical observables.

A. Integrated fluxes

The integrated fluxes are depicted in Fig. 7 for the ΛBS configurations, and in Fig. 8 for the SBS ones. Given that the orbital radius of the isotropically emitting source is considered to be constant, the integrated fluxes for a whole orbit resemble a torus-like emission. For the ΛBS models, one verifies that the results are qualitatively similar to the ones obtained in a previous publication [34] for bosonic stars without self-interactions, a result that is somewhat expected since the space-time properties of these configurations are also similar, i.e., these stars are not compact enough to have either a light ring or an ISCO, and they do not feature event horizons either. Indeed, for small observation angles one can only observe the primary track of the hot spot. The secondary track eventually becomes observable as one increases the compactness of the star and/or the observation angle. Such a secondary track features two components, the usual secondary image also observed in black hole space-times, and a plunge-through image

corresponding to the photons crossing the interior of the bosonic star before reaching the observer. The latter component is absent in black hole space-times due to the existence of an event horizon and consequent impossibility of photons to escape from the interior of the space-time.

For the SBS models, more interesting and qualitatively different results arise. Whereas for the SBS1 model the integrated flux images are again qualitatively similar to the ones previously obtained for the ΛBS models, i.e., only the primary track is observed for a low inclination angle and the secondary track, composed by the usual secondary plus the plunge-through components, eventually arises as one increases the inclination angles. However, the situation drastically changes for the SBS2 and the SBS3 models. Indeed, for such models not only the secondary track is always present, but also several additional tracks can be observed. For the SBS2 model, for an observation angle of $\theta = 20°$, two additional closed tracks can be observed besides the primary image. These two extra tracks eventually merge into a single secondary track with two components, the usual secondary and the plunge-through components, for larger observation angles. The SBS3 model features an even more complex structure of sub-images: a third additional track and the light-ring contributions can also be observed for low observation angles, and these contributions do not merge as one increases the observation angle.

These results indicate that the qualitative properties of the observed integrated fluxes depend strongly on the compactness of these horizonless compact objects,
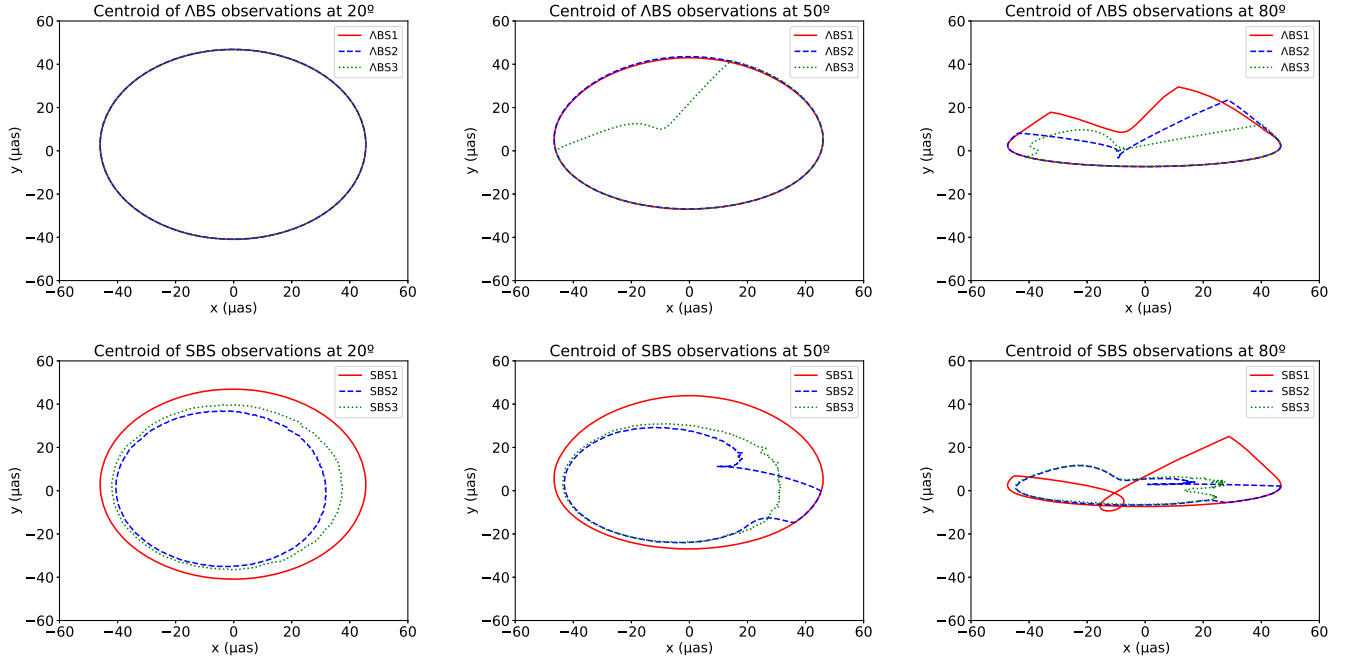
FIG. 10. Centroid of the observations in μas for the ΛBS models (top row) and the SBS models (bottom row) for an observation inclination of $\theta = 20°$ (left column), $\theta = 50°$ (middle column), and $\theta = 80°$ (right column).

a feature that was already hinted by a previous publication on relativistic fluid stars [45]. Three different regimes can thus be identified:

(i) If the light deflection is not strong enough, the secondary track can only be observed for certain inclination angles, i.e., there is a critical observation angle $\theta_c^{(1)}$ such that if $\theta < \theta_c^{(1)}$ the secondary track is absent.

(ii) For a stronger light deflection, the secondary track is present independently of the observation angle but its two components, the usual secondary and the plunge through, might be observed as independent tracks for some observation angles, i.e., there is another critical observation angle $\theta_c^{(2)}$, such that if $\theta < \theta_c^{(2)}$ the secondary and the plunge-through components are independent tracks, and if $\theta > \theta_c^{(2)}$ the secondary and the plunge-through components merge into a single secondary track.

(iii) For a very large light deflection, there is a further split of the secondary track into three independent tracks, independently of the observation angle.

In this work, the third component of the secondary and the light-ring components are only visible for the SBS3 model. We note, however, that this does not mean that these two contributions always arise simultaneously. Indeed, in the previous work on relativistic fluid spheres referenced above, several examples for which the light-ring contributions are present without the third splitting of the secondary track are provided.

B. Astrometrical properties

The qualitative behavior of both the magnitude m_k (depicted in Fig. 9 for both the ΛBS and SBS configurations) and the centroid $\vec{c}_k$ (depicted in Fig. 10) are strongly dependent on the subimage structure of the observation. If a single track, i.e., the primary track, is observable, the magnitude of the observation features a single peak caused by the Doppler shifting due to the orbital motion, whereas the centroid of the observation follows the position of the primary image, as it happens for all of the ΛBS models and for an observation angle of 20°. The slight difference in the height of these peaks is caused by the differences in the angular velocity of the hot spot, which is slightly larger for the more compact configurations.

If at some point of the orbit a secondary image appears, one observes an increase in the magnitude of the observation caused by the extra photons arising at the observer from the secondary image, and the centroid of the observation is shifted towards the secondary image. This effect can be clearly observed for the ΛBS3 model for an observation inclination of $\theta = 50°$, as well as the ΛBS1, ΛBS2, and SBS1 for an observation inclination of $\theta = 80°$. Note that if the effects of light deflection are strong enough to break the two components of the secondary track into two separated images, the secondary and the plunge through, then the additional peak in the magnitude breaks into several subpeaks, corresponding to the instants in which the secondary image appears and splits into two components, then both achieve a maximum of luminosity, and finally they merge and disappear. Depending on the

relative intensity of these two components, the behavior of the centroid might follow a more complicated trajectory, as it happens for the ΛBS3 model at an observation angle of $\theta = 80°$ and for the SBS2 model at both $\theta = 50°$ and $\theta = 80°$.

When the light deflection is strong enough to induce the appearance of additional secondary tracks, the complexity of the behavior of the magnitude and the centroid increases. For low-inclination observations for which the additional tracks are present and do not merge, one observes that the centroid still follows an approximately elliptical curve, but this curve is smaller than in the case in which a single primary image is present, as the secondary contributions shift the centroid towards the center of the observation. Furthermore, for the magnitude, although it still features a single peak, the latter is smaller than in the case of a single primary image, as the photons corresponding to the secondary image arise to the observer from a trajectory crossing the central object through the opposite of the primary image, and thus contribute negatively to the Doppler shift. These effects are observed for the SBS2 model at $\theta = 20°$ and the SBS3 model for both $\theta = 20°$ and $\theta = 50°$.

Finally, it is interesting to note that even though all observable tracks in the SBS3 model are visible independently of the observation angle, the contribution of the secondary tracks to the total flux increases with the observation angle, being particularly relevant in the region of the observers' screen opposite to the primary track. As a consequence, and even though the secondary tracks are always present, one can still observe the appearance of additional peaks in the magnitude and consequent shifting of the centroid for the SBS3 model at an observation inclination of $\theta = 80°$. The main difference between this situation and the one described previously for which the secondary image appears at some point in the orbit, splits into two components, merges, and disappears again, is that in that situation one observes three additional peaks in the magnitude, whereas in this case only two additional peaks are present. Note that for all of the SBS3 model observations, both the magnitude and the centroid present a slight noise caused by the light-ring contribution.

IV. ACCRETION DISKS

A. Intensity profiles

Let us now turn to the observational properties of optically thin accretion disks around the bosonic stars considered previously. For this purpose, we recur to a *Mathematica*-based ray-tracing code previously used in several other publications [46,47], where the (infinitesimally thin) accretion disk at the equatorial plane is modeled by a monochromatic intensity profile. To model these intensity profiles, we recur to the recently introduced Gralla-Lupsasca-Marrone (GLM) model [48], whose main interest is the

fact that its predictions are in a close agreement with those of general relativistic magneto-hydrodynamics simulations of astrophysical accretion disks [49]. The intensity profile of the GLM model is given by

$$I_e(r; \gamma, \beta, \sigma) = \frac{\exp\left\{-\frac{1}{2}\left[\gamma + \operatorname{arcsinh}\left(\frac{r-\beta}{\sigma}\right)\right]^2\right\}}{\sqrt{(r-\beta)^2 + \sigma^2}}, \quad (29)$$

where γ, β and σ are free parameters controlling the shape of the emission profile, namely the rate of increase, a radial translation, and the dilation of the profile, respectively. These parameters can be adjusted in order to select adequate intensity profiles for the models under study. For the purpose of this work, we select two different GLM models to model the intensity profile of the accretion disk, which we motivate in what follows:

(i) Given that all of the bosonic star configurations considered in this work feature stable orbital regimes close to the center of the star $r = 0$, and under the assumption that the matter composing the accretion disk interacts only weakly with the fundamental fields composing the star, it is fair to assume that the intensity profile of the accretion disk increases monotonically from infinity downwards and peaks at the center. We denote this as the *Central* accretion disk model, which is described by the parameters $\gamma = \beta = 0$ and $\sigma = 2M$ in the GLM model above.

(ii) On the other hand, the SBS configurations feature marginally stable circular orbits at $r_{MS} \sim 6M$ (cf. Fig. 4). Given that circular orbits become unstable in a region of $r_o < r_{MS}$, and provided that the SBS models explored here have a maximum in Ω_o, it is reasonable to consider an intensity profile of the accretion disk which increases monotonically down to $r = r_{MS}$, where it peaks, and then abruptly decreases for $r < r_{MS}$. This structure should be similar to the ones found in Ref. [22], which shows through magneto-hydrodynamics simulations that some accretion disks in boson stars could have inner edges. We denote this as the *ISCO* accretion disk model, given the similarity to the black hole case, being described by the parameters $\gamma = -2$, $\beta = 6M$, and $\sigma = M/4$. Note that the r_{ISCO} for the three SBS configurations is not exactly $6M$ and differs depending on the model. Nevertheless, to allow for a same-ground comparison of the results between these two models, we take $\beta = 6M$ for every configuration.

The emitted intensity profiles I_e for the Central and ISCO disk models are plotted in Fig. 11. In what follows, the Central disk model is used in the background of all bosonic star configurations, i.e., for both ΛBS and SBS, whereas the ISCO disk model is used only for those configurations which feature an ISCO, i.e., only the SBS ones.
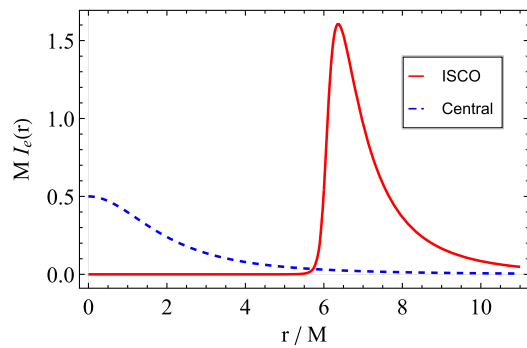
FIG. 11. Emitted intensity profiles for the GLM model given in Eq. (29) for two different combinations of parameters: the Central model with $\gamma = \beta = 0$ and $\sigma = 2M$; and the ISCO model with $\gamma = -2$, $\beta = 6M$, and $\sigma = M/4$.

We note that all of the results that follow in the remainder of this section concern solely stationary accretion disk configurations in equilibrium around the central bosonic star, while dynamical accretion effects are neglected. It has been shown [22] that dynamical magneto-hydrodynamics and radiative transfer effects in bosonic star space-times induce additional observational imprints which further differentiate these space-times from their black hole counterparts, resulting in a more diffuse shadow boundary with a lower contrast in comparison with a black hole of the same mass. These effects occur mainly due to the absence of the event horizon and to the existence of stable orbits in the inner regions of the space-time, as previously mentioned in the discussion of Fig. 4. One can thus think of the results that follow as representative of the initial stages of accretion towards the central bosonic star, before such dynamical effects had taken place.

B. Axial observations

The intensity profiles given in Fig. 11 correspond to the reference frame of the emitter I_e, i.e., the accretion disk, where the photons are emitted with a given frequency, say ν_e. In the reference frame of the observer, the observed frequency ν_0 is redshifted with respect to the emitted one, with $\nu_0 = \sqrt{-g_{tt}}\nu_e$. Consequently, the intensity profile in

the reference frame of the observer I_0 is affected by the shape of the background metric and takes the form

$$I_0(r) = A^2(r)I_e(r). \tag{30}$$

The observed intensity profiles for the combinations of accretion disk models and bosonic star configurations outlined previously are given in Fig. 12, whereas the corresponding observed axial images (i.e., as observed from the axis of symmetry of the accretion disk) for the Central and ISCO disk models are provided in Figs. 13 and 14, respectively.

For the Central disk model, we verify that for every ΛBS configuration, as well as for the SBS1 configuration, the effects of the gravitational redshift are not strong enough to induce a decrease in the central intensity peak, and thus the observed images for these models present similar qualitative properties, more precisely a central blob of radiation. However, for the SBS2 and SBS3 configurations, one verifies that the effects of the gravitational redshift induce a strong dimming in the central peak, leading to a maximum of intensity away from the center. This dimming of intensity produces a shadowlike feature for these two models, inducing a brightness depression region in the center of the observed images. Furthermore, one also verifies that for these two models the light deflection is strong enough to produce additional contributions in the observed images caused by photons that have revolved around the central object more than a half orbit. These are known as the secondary images, similar to those already found in the hot spots above, and produce the additional peaks of intensity visible for the SBS2 and SBS3 configurations. Furthermore, one can also observe a thin peak in the intensity profile of the SBS3 configuration, corresponding to the light ring, which is also visible as a thin intense circle in the observed image.

As for the ISCO disk model, given that the intensity profiles in the reference frame of the emitter are truncated at a finite radius, namely $r = 6M$, all observed images produced with this model feature a central dark region independently of the bosonic star configuration considered as a background. Nevertheless, bosonic stars with different
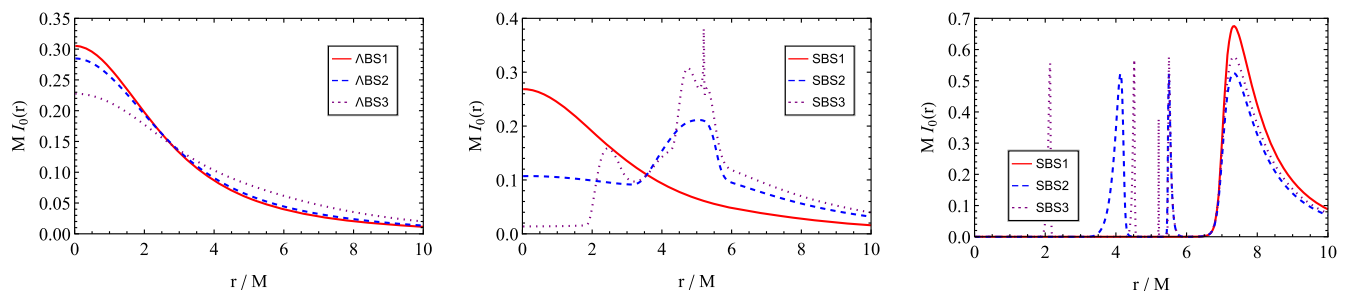

FIG. 12. Observed intensity profiles for the ΛBS configurations with the Central disk model (left panel), for the SBS configurations with the Central disk model (middle panel), and for the SBS boson stars with the ISCO disk model (right panel).
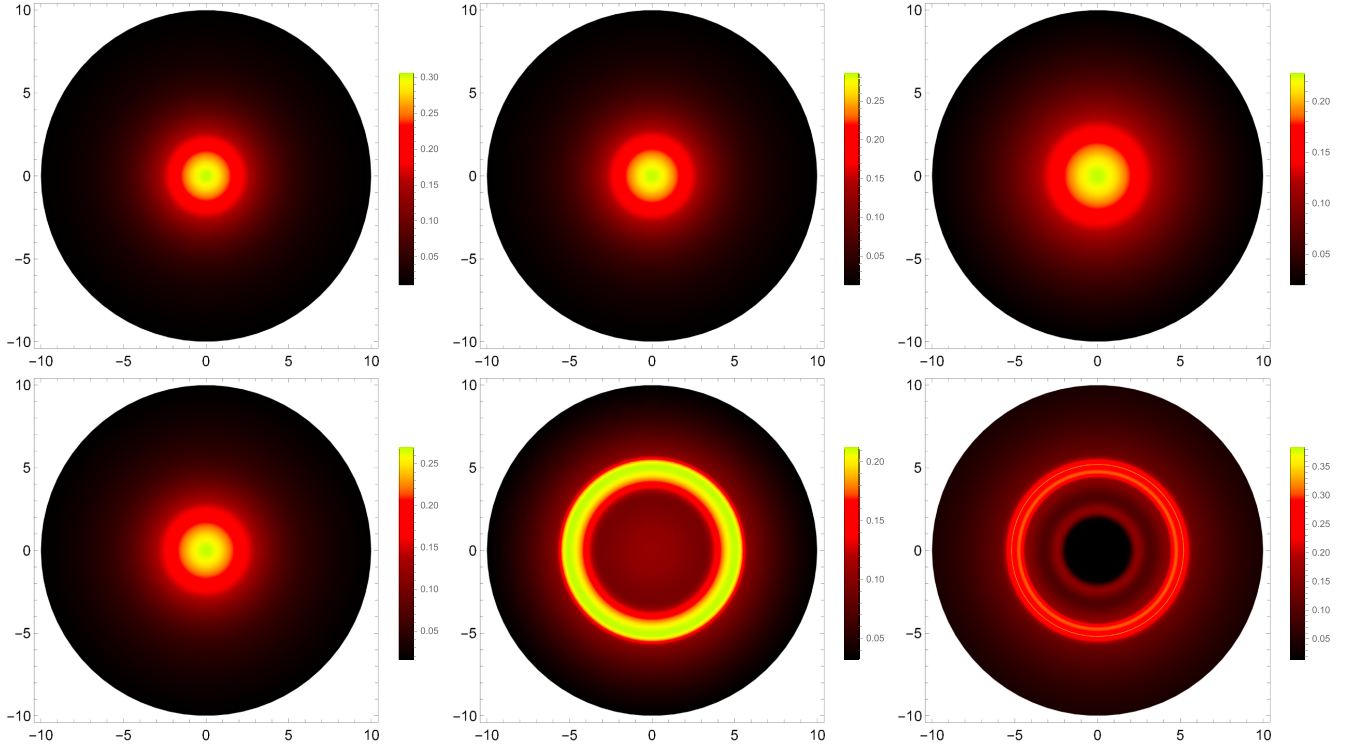
FIG. 13.   Shadow images for the ΛBS (top row) and SBS (bottom row) configurations with the Central disk model, as seen from an inclination angle of $\theta = 0°$.
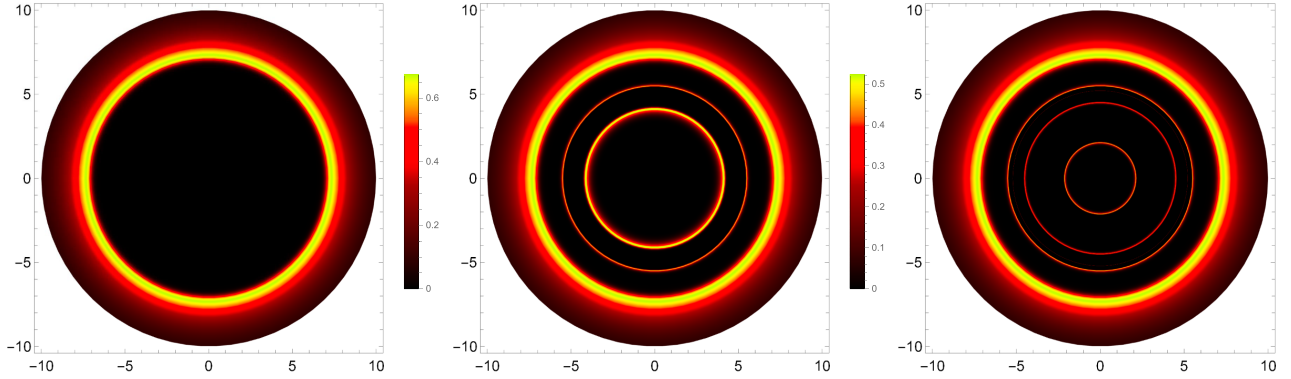

FIG. 14.   Shadow images for the SBS configurations with the ISCO disk model, as seen from an inclination angle of $\theta = 0°$.

compactness and geodesic structures feature qualitatively different behaviors. For the SBS1 configuration, the light deflection is not strong enough to produce secondary images, and thus the observed intensity profile features a single peak, which is translated into the observed image as a single ring and a dark shadow without any additional features. When the light deflection is strong enough to produce a secondary image, additional peaks of intensity start appearing in the observed intensity profiles, which contribute with extra circular contributions to the observed image inside the previous shadow. The number of secondary images depends on the metric chosen as a background, varying from a single secondary image [45] to several, as it

happens for the SBS2 and SBS3 models. In particular, for the SBS3 configuration, one observes three additional secondary peaks in the observed intensity, as well as the light-ring contribution, which are translated as four additional circular contributions in the observed image, inside the shadow.

The results described above indicate that the ΛBS configurations, along with the SBS1 configuration with the Central disk model, are not compact enough to reproduce the expected observable properties of black hole space-times, more specifically, the shadow observed in the images of the supermassive objects in the center of M87 and Sgr A* galaxies, and thus they do not correspond to
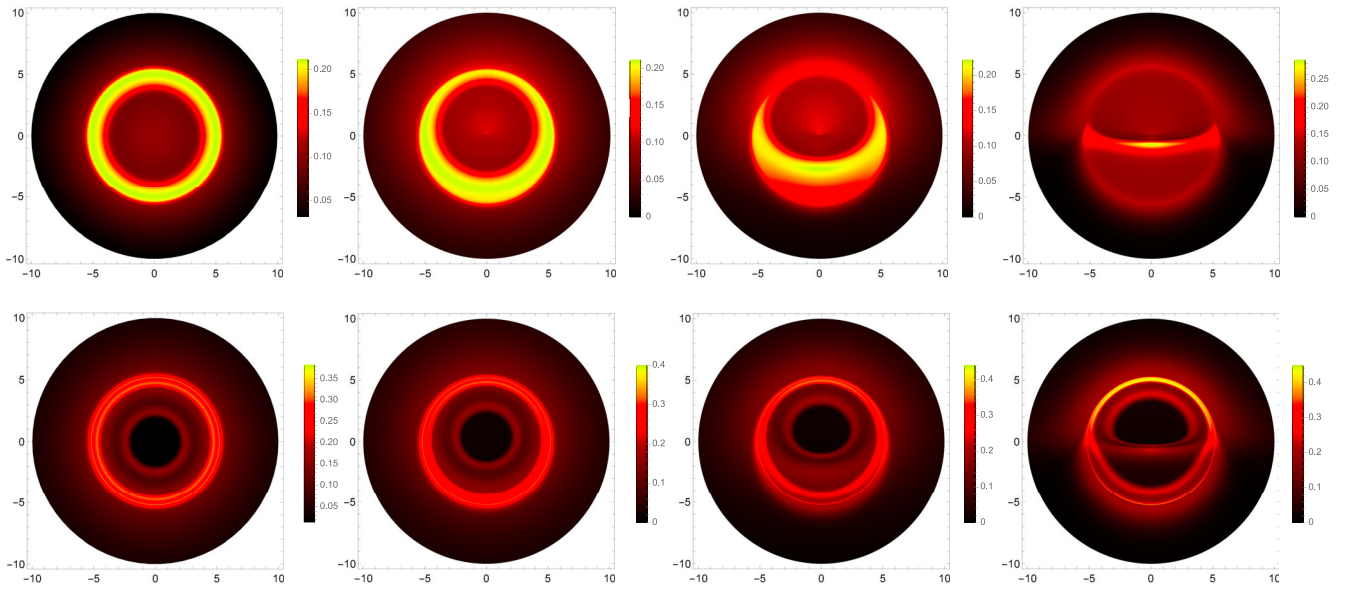
FIG. 15.   Shadow images for the SBS2 (top row) and SBS3 (bottom row) bosonic stars with the Central disk model, as seen from inclination angles of $\theta = \{0°, 20°, 50°, 80°\}$, from left to right.
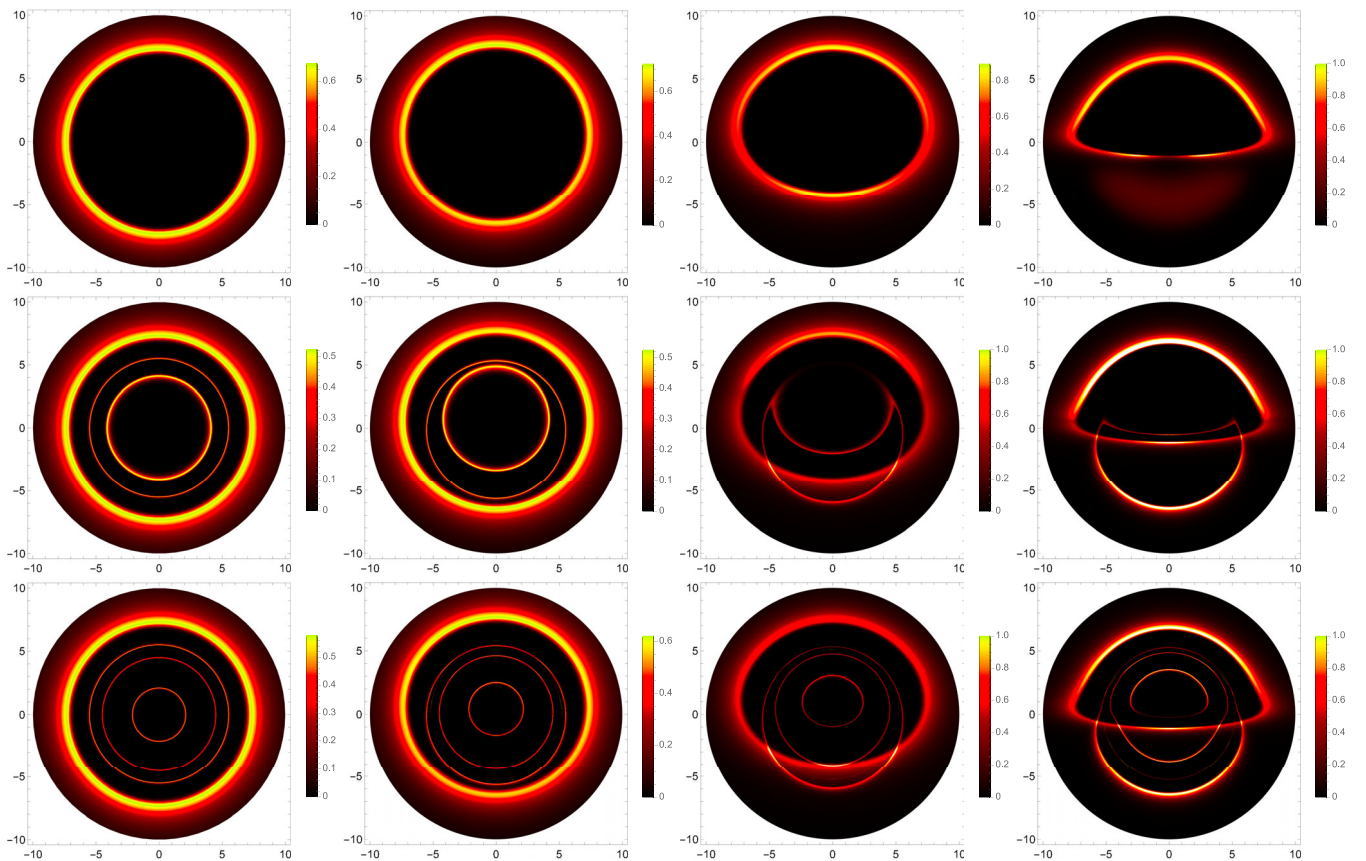

FIG. 16.   Shadow images for the SBS1 (top row), SBS2 (middle row), and SBS3 (bottom row) configurations with the ISCO disk model, as seen from inclination angles of $\theta = \{0°, 20°, 50°, 80°\}$, from left to right.

adequate models for black hole mimickers in this astrophysical context, provided that the universality of black hole metrics holds. On the other hand, the SBS2 and SBS3 configurations, along with the SBS1 configuration with the ISCO disk model, do produce shadowlike features in the observed images, and are thus potentially suitable candidates for black hole mimickers in this context and deserve a more careful analysis.

C. Inclined observations

For the combinations of accretion disk models and bosonic star configurations deemed more astrophysically relevant as black hole mimickers in the previous section, we have produced additional images considering observers standing at inclination angles of $\theta = \{20°, 50°, 80°\}$. As a comparison to our analysis here, observed images for the same inclination angles in the background of a Schwarzschild black hole can be found, e.g., in Ref. [45]. The observed images for SBS2 and SBS3 with the Central disk model are given in Fig. 15, whereas the observed images for all SBS configurations with the ISCO disk model are given in Fig. 16.

These results indicate that, even though the SBS2 configuration with a Central disk model presents a central dimming of radiation when observed axially, the contrast between the central dimming and the intensity of the secondary peak smoothens out as one increases the observation inclination, resulting in an observed image at high inclinations that differs drastically from the black hole scenario, see Ref. [45]. The same does not apply to the SBS3 model, for which a dark shadowlike region with a strong contrast with respect to the surrounding region near the light-ring is present independently of the inclination observation. It is worth mentioning, however, that the size of the shadow of the SBS3 configuration is significantly smaller than its black hole scenario counterpart, mainly due to the secondary contributions that appear inside the light ring, which in turn may trouble the compatibility of such models with calibrated observations of shadows' radius [32]. For the ISCO disk model, again one verifies that the SBS1, even though it produces a shadow similar to that of a black hole from an axial inclination perspective since light deflection is not strong enough to produce a secondary image, the resulting observation at high inclinations differs drastically from that of a black hole. The SBS2 and SBS3, on the other hand, do produce observed images featuring secondary images, and thus are more closely related to their black hole counterparts. Nevertheless, one can still enumerate several qualitative differences between these models and the black hole scenario, namely the plunge-through image in the absence of a light in the SBS2, a feature similar to what was previously found for boson stars without self-interactions [50], and several additional secondary tracks inside the light for SBS3, features that can effectively act as

observational discriminators between boson stars of this kind and black hole space-times.

V. CONCLUSION

In this work we have analyzed the observational properties of bosonic stars with self-interactions being orbited by isotropically emitting sources and optically thin accretion disks. In particular, we studied bosonic stars with quartic interaction terms (ΛBS models), as well as solitonic boson stars with sixth-order interaction terms (SBS models). The SBS models, and particularly the SBS3 model which is compact enough to develop a light-ring pair, were shown to more closely reproduce the observable features of black hole space-times and thus provide more suitable models for black hole mimickers.

Indeed, we have shown that the light deflection effects in the ΛBS models are not strong enough to produce any qualitative differences with respect to the observations from boson and Proca stars without self-interactions, i.e., the same astrometric effects for orbital motion, e.g., the shifting of the centroid and additional peaks of magnitude when the secondary tracks are present, as well as a weak central intensity dimming in accretion disk models that extend all the way down to the center of these configurations. We thus conclude that these models can hardly be taken as strong candidates to represent current observations from the EHT and GRAVITY collaborations, and are thus not adequate to describe supermassive compact objects found in galactic centers.

As for the SBS models, we verified that these are potentially relevant in this astrophysical context, provided that they are compact enough. For the least compact of these configurations, namely SBS1, the observational properties are similar to the ones of ΛBS configurations and bosonic stars without self-interactions, and thus inadequate to describe the images of the objects at the galactic centers. However, this is not true for the SBS2 and SBS3 models. Indeed, for the latter models one observes a dimming of intensity in the central region of the accretion disk caused by the gravitational redshift, resulting in a shadowlike feature similar to that of a black hole. For the SBS3 model, this dark region is more pronounced and remains visible for any inclination angle, although being slightly smaller than its black hole counterpart. Furthermore, both the SBS2 and SBS3 configurations present additional secondary images for both the orbital motion of a hot spot and the optically thin accretion disk, and the SBS3 configuration features also light-ring contributions.

The qualitative differences between the SBS2 and SBS3 models with respect to the black hole scenario indicate that, even though these models are virtually indistinguishable from a black hole given the lack of enough resolution in current EHT observations to resolve secondary images in the main ring of radiation, an eventual upgrade in these observatories (via e.g., the ngEHT) and an increase in the quality and resolution of the observed images may allow

the detection of these additional contributions to the image in order to conclusively infer the nature of these super-massive compact objects.

ACKNOWLEDGMENTS

[1] Roy P. Kerr, Gravitational Field of a Spinning Mass as an Example of Algebraically Special Metrics, Phys. Rev. Lett. **11**, 237 (1963).

[2] Pankaj S. Joshi, *Gravitational Collapse and Spacetime Singularities*, Cambridge Monographs on Mathematical Physics (Cambridge University Press, Cambridge, England, 2007).

[3] B. P. Abbott *et al.*, Observation of Gravitational Waves from a Binary Black Hole Merger, Phys. Rev. Lett. **116**, 061102 (2016).

[4] B. P. Abbott *et al.*, GW170817: Observation of Gravitational Waves from a Binary Neutron Star Inspiral, Phys. Rev. Lett. **119**, 161101 (2017).

[5] Kazunori Akiyama *et al.*, First M87 event horizon telescope results. I. The shadow of the supermassive black hole, Astrophys. J. Lett. **875**, L1 (2019).

[6] Kazunori Akiyama *et al.*, First Sagittarius A* event horizon telescope results. I. The shadow of the supermassive black hole in the center of the Milky Way, Astrophys. J. Lett. **930**, L12 (2022).

[7] Clifford M. Will, The confrontation between general relativity and experiment, Living Rev. Relativity **17**, 4 (2014).

[8] Kent Yagi and Leo C. Stein, Black hole based tests of general relativity, Classical Quantum Gravity **33**, 054001 (2016).

[9] Vitor Cardoso and Paolo Pani, Testing the nature of dark compact objects: A status report, Living Rev. Relativity **22**, 4 (2019).

[10] Steven L. Liebling and Carlos Palenzuela, Dynamical boson stars, Living Rev. Relativity **15**, 6 (2012).

[11] Richard Brito, Vitor Cardoso, and Hirotada Okawa, Accretion of Dark Matter by Stars, Phys. Rev. Lett. **115**, 111301 (2015).

[12] Richard Brito, Vitor Cardoso, Caio F. B. Macedo, Hirotada Okawa, and Carlos Palenzuela, Interaction between bosonic dark matter and stars, Phys. Rev. D **93**, 044045 (2016).

[13] Richard Brito, Vitor Cardoso, Carlos A. R. Herdeiro, and Eugen Radu, Proca stars: Gravitating Bose-Einstein condensates of massive spin 1 particles, Phys. Lett. B **752**, 291 (2016).

[14] Zheng Cao, Alejandro Cardenas-Avendano, Menglei Zhou, Cosimo Bambi, Carlos A. R. Herdeiro, and Eugen Radu, Iron Kα line of boson stars, J. Cosmol. Astropart. Phys. 10 (2016) 003.

[15] R. Sharma, S. Karmakar, and S. Mukherjee, Boson star and dark matter, arXiv:0812.3470.

[16] Lam Hui, Jeremiah P. Ostriker, Scott Tremaine, and Edward Witten, Ultralight scalars as cosmological dark matter, Phys. Rev. D **95**, 043541 (2017).

[17] Carlos Palenzuela, Paolo Pani, Miguel Bezares, Vitor Cardoso, Luis Lehner, and Steven Liebling, Gravitational wave signatures of highly compact boson star binaries, Phys. Rev. D **96**, 104058 (2017).

[18] Vitor Cardoso and Paolo Pani, Tests for the existence of black holes through gravitational wave echoes, Nat. Astron. **1**, 586 (2017).

[19] A. M. Pombo and I. Saltas, A Sun-like star orbiting a boson star, Mon. Not. R. Astron. Soc. **524**, 4083 (2023).

[20] Farruh Atamurotov, Ahmadjon Abdujabbarov, and Bobomurat Ahmedov, Shadow of rotating non-Kerr black hole, Phys. Rev. D **88**, 064004 (2013).

[21] F. H. Vincent, Z. Meliani, P. Grandclement, E. Gourgoulhon, and O. Straub, Imaging a boson star at the Galactic Center, Classical Quantum Gravity **33**, 105015 (2016).

[22] Hector Olivares, Ziri Younsi, Christian M. Fromm, Mariafelicia De Laurentis, Oliver Porth, Yosuke Mizuno, Heino Falcke, Michael Kramer, and Luciano Rezzolla, How to tell an accreting boson star from a black hole, Mon. Not. R. Astron. Soc. **497**, 521 (2020).

[23] Askar B. Abdikamalov, Ahmadjon A. Abdujabbarov, Dimitry Ayzenberg, Daniele Malafarina, Cosimo Bambi, and Bobomurat Ahmedov, Black hole mimicker hiding in the shadow: Optical properties of the γ metric, Phys. Rev. D **100**, 024014 (2019).

[24] F. H. Vincent, M. Wielgus, M. A. Abramowicz, E. Gourgoulhon, J. P. Lasota, T. Paumard, and G. Perrin, Geometric modeling of M87* as a Kerr black hole or a non-Kerr compact object, Astron. Astrophys. **646**, A37 (2021).

[25] Carlos A. R. Herdeiro, Alexandre M. Pombo, Eugen Radu, Pedro V. P. Cunha, and Nicolas Sanchis-Gual, The imitation game: Proca stars that can mimic the Schwarzschild shadow, J. Cosmol. Astropart. Phys. 04 (2021) 051.

[26] Haroldo C. D. Lima, Jr., Luís C. B. Crispino, Pedro V. P. Cunha, and Carlos A. R. Herdeiro, Can different black holes cast the same shadow?, Phys. Rev. D **103,** 084040 (2021).

[27] Pedro V. P. Cunha and Carlos A. R. Herdeiro, Stationary Black Holes and Light Rings, Phys. Rev. Lett. **124,** 181101 (2020).

[28] Samuel E. Gralla, Daniel E. Holz, and Robert M. Wald, Black hole shadows, photon rings, and lensing rings, Phys. Rev. D **100,** 024018 (2019).

[29] Michael D. Johnson *et al.*, Universal interferometric signatures of a black hole's photon ring, Sci. Adv. **6,** eaaz1310 (2020).

[30] Maciek Wielgus, Photon rings of spherically symmetric black holes and robust tests of non-Kerr metrics, Phys. Rev. D **104,** 124058 (2021).

[31] Andrew Chael, Michael D. Johnson, and Alexandru Lupsasca, Observing the inner shadow of a black hole: A direct view of the event horizon, Astrophys. J. **918,** 6 (2021).

[32] Sunny Vagnozzi *et al.*, Horizon-scale tests of gravity theories and fundamental physics from the event horizon telescope image of Sagittarius A*, Classical Quantum Gravity **40,** 165007 (2023).

[33] Jesse Vos, Monika Moscibrodzka, and Maciek Wielgus, Polarimetric signatures of hot spots in black hole accretion flows, Astron. Astrophys. **668,** A185 (2022).

[34] João Luís Rosa, Paulo Garcia, Frédéric H. Vincent, and Vitor Cardoso, Observational signatures of hot spots orbiting horizonless objects, Phys. Rev. D **106,** 044031 (2022).

[35] M. Colpi, S. L. Shapiro, and I. Wasserman, Boson Stars: Gravitational Equilibria of Self-Interacting Scalar Fields, Phys. Rev. Lett. **57,** 2485 (1986).

[36] Pau Amaro-Seoane, Juan Barranco, Argelia Bernal, and Luciano Rezzolla, Constraining scalar fields with stellar kinematics and collisional dark matter, J. Cosmol. Astropart. Phys. 11 (2010) 002.

[37] T. D. Lee, Soliton stars and the critical masses of black holes, Phys. Rev. D **35,** 3637 (1987).

[38] T. D. Lee and Y. Pang, Nontopological solitons, Phys. Rep. **221,** 251 (1992).

[39] Vitor Cardoso, Caio F. B. Macedo, Kei-ichi Maeda, and Hirotada Okawa, ECO-spotting: Looking for extremely compact objects with bosonic fields, Classical Quantum Gravity **39,** 034001 (2022).

[40] Caio F. B. Macedo, Paolo Pani, Vitor Cardoso, and Luís C. B. Crispino, Astrophysical signatures of boson stars: Quasinormal modes and inspiral resonances, Phys. Rev. D **88,** 064046 (2013).

[41] Pedro V. P. Cunha, Emanuele Berti, and Carlos A. R. Herdeiro, Light-Ring Stability for Ultracompact Objects, Phys. Rev. Lett. **119,** 251102 (2017).

[42] Pedro V. P. Cunha, Carlos Herdeiro, Eugen Radu, and Nicolas Sanchis-Gual, Exotic Compact Objects and the Fate of the Light-Ring Instability, Phys. Rev. Lett. **130,** 061401 (2023).

[43] Tom Stratton and Sam R. Dolan, Rainbow scattering of gravitational plane waves by a compact body, Phys. Rev. D **100,** 024007 (2019).

[44] F. H. Vincent, T. Paumard, E. Gourgoulhon, and G. Perrin, GYOTO: A new general relativistic ray-tracing code, Classical Quantum Gravity **28,** 225011 (2011).

[45] João Luís Rosa, Observational properties of relativistic fluid spheres with thin accretion disks, Phys. Rev. D **107,** 084048 (2023).

[46] Merce Guerrero, Gonzalo J. Olmo, Diego Rubiera-Garcia, and Diego Sáez-Chillón Gómez, Shadows and optical appearance of black bounces illuminated by a thin accretion disk, J. Cosmol. Astropart. Phys. 08 (2021) 036.

[47] Gonzalo J. Olmo, Joao Luis Rosa, Diego Rubiera-Garcia, and Diego Saez-Chillon Gomez, Shadows and photon rings of regular black holes and geonic horizonless compact objects, Classical Quantum Gravity **40,** 174002 (2023).

[48] Samuel E. Gralla, Alexandru Lupsasca, and Daniel P. Marrone, The shape of the black hole photon ring: A precise test of strong-field general relativity, Phys. Rev. D **102,** 124004 (2020).

[49] Frederic H. Vincent, Samuel E. Gralla, Alexandru Lupsasca, and Maciek Wielgus, Images and photon ring signatures of thick disks around black holes, Astron. Astrophys. **667,** A170 (2022).

[50] João Luís Rosa and Diego Rubiera-Garcia, Shadows of boson and Proca stars with thin accretion disks, Phys. Rev. D **106,** 084004 (2022).